

# Ferritin Protein Regulates the Degradation of Iron Oxide Nanoparticles

Jeanne Volatron, Florent Carn, Jelena Kolosnjaj-Tabi, Yasir Javed, Quoc Lam Vuong, Yves Gossuin, Christine Ménager, Nathalie Luciani, Gaëlle Charron, Miryana Hémadi, Damien Alloyeau,\* and Florence Gazeau\*

**P**roteins implicated in iron homeostasis are assumed to be also involved in the cellular processing of iron oxide nanoparticles. In this work, the role of an endogenous iron storage protein—namely the ferritin—is examined in the remediation and biodegradation of magnetic iron oxide nanoparticles. Previous *in vivo* studies suggest the intracellular transfer of the iron ions released during the degradation of nanoparticles to endogenous protein cages within lysosomal compartments. Here, the capacity of ferritin cages to accommodate and store the degradation products of nanoparticles is investigated *in vitro* in the physiological acidic environment of the lysosomes. Moreover, it is questioned whether ferritin proteins can play an active role in the degradation of the nanoparticles. The magnetic, colloidal, and structural follow-up of iron oxide nanoparticles and proteins in lysosome-like medium confirms the efficient remediation of potentially harmful iron ions generated by nanoparticles within ferritins. The presence of ferritins, however, delays the degradation of particles due to a complex colloidal behavior of the mixture in acidic medium. This study exemplifies the important implications of intracellular proteins in processes of degradation and metabolization of iron oxide nanoparticles.

Dr. J. Volatron, F. Carn, Dr. J. Kolosnjaj-Tabi, Dr. N. Luciani,  
Dr. G. Charron, Dr. F. Gazeau  
Laboratoire Matières et Systèmes Complexes  
UMR 7057 CNRS/Université Paris Diderot  
Sorbonne Paris Cité  
10 rue Alice Domon et Léonie Duquet, 75205 Paris Cedex 13, France  
E-mail: florence.gazeau@univ-paris-diderot.fr

Dr. Y. Javed, Dr. D. Alloyeau  
Laboratoire Matériaux et Phénomènes Quantiques  
UMR 7162 CNRS/Université Paris Diderot  
Sorbonne Paris Cité  
10 rue Alice Domon et Léonie Duquet, 75205 Paris Cedex 13, France  
E-mail: damien.alloyeau@univ-paris-diderot.fr

Dr. Y. Javed  
Department of Physics  
University of Agriculture  
Faisalabad, Pakistan

Dr. Q. L. Vuong, Prof. Y. Gossuin  
Service de Physique Biomédicale  
Université de Mons  
20 Place du Parc, 7000 Mons, Belgium  
Prof. C. Ménager  
Laboratoire PHENIX  
UMR 7195  
CNRS/Université Pierre et Marie Curie/ESPCI  
4 place Jussieu, 75252 Paris Cedex 05, France  
Dr. M. Hémadi  
ITODYS, Interfaces, Traitements, Organisation et  
Dynamique des Systèmes  
UMR 7086 CNRS/Université Paris Diderot  
Sorbonne Paris Cité  
15 rue Jean-Antoine de Baïf, 75205 Paris Cedex 13, France



DOI: 10.1002/sml.201602030

## 1. Introduction

The use of inorganic nanoparticles (NPs) in preclinical research is rapidly expanding, paving the way for new imaging and therapeutic strategies. Particularly magnetic NPs, mostly made of iron oxide (IO), display attractive functionalities making them the most popular inorganic NPs with applications in Magnetic Resonance Imaging (MRI), Magnetic Particle Imaging, magnetic manipulation of drug delivery systems and cells, tissue engineering, or magnetic hyperthermia, to cite just a few.<sup>[1]</sup> Remarkably, iron oxide NPs (IONPs) are considered efficient and safe and already found their way into clinics.<sup>[2]</sup> In contrast to the majority of metallic NPs, their biocompatibility relies on possible degradation in the body and recycling by iron metabolism pathway.<sup>[3]</sup> Recent studies evaluating the fate of IONPs *in vivo* demonstrated that IONPs were indeed locally degraded in the lysosomes of splenic and hepatic macrophages while they lose their superparamagnetic properties over periods of months after injection.<sup>[4]</sup> Radioactive labeling of IONPs showed that <sup>59</sup>Fe released from NPs appeared in the hemoglobin of newly formed erythrocytes one week after injection, confirming intracellular degradation and channeling of iron into the physiological transport pathways for iron.<sup>[5]</sup> A substantial part of the radiolabel was also retained in organs, suggesting intracellular storage of iron. Importantly, the gene expression of ferritin, the endogenous iron storage protein, and of other proteins involved in iron homeostasis, was upregulated after cell internalization of IONPs.<sup>[3b,6]</sup> Ferritin consists of a protein shell (called apoferritin (ApoF)) of 24 subunits with an outer diameter of 12 nm and a cavity of 8 nm diameter, able to store up to 4500 atoms of iron (iron-filled ferritin is called holoferritin (HoloF)).<sup>[7]</sup> Ferritin is a multifunctional protein that does not only detoxify, store, and transport iron, but is also implicated in several metabolic processes.<sup>[8]</sup> Ferritin is able to store excess iron, which is not immediately required by cells for metabolic processes, in a readily available nontoxic form.<sup>[9]</sup> It thus protects the cell from the toxic effects of hydroxyl radicals HO<sup>•</sup> generated by the Fenton reaction initiated by free Fe<sup>2+</sup> ions.<sup>[10]</sup> Given the ubiquitous presence of ferritin close to intracellular IONPs demonstrated by high-resolution transmission electron microscopy (HRTEM) of organs,<sup>[4c]</sup> it has been suggested that ferritin could be involved in the degradation mechanism of IONPs *in vivo* by recycling iron ions released by NPs.<sup>[4a,11]</sup> Indeed, the magnetic properties of the original particles in spleen turned to that of the iron-filled ferritin over months following administration.<sup>[4a,c,f]</sup> Nonetheless, the interplay between IONPs and ferritin and their intracellular crosstalk remain unclear. Overall, while it has been generally accepted that NPs extensively interact with intracellular proteins,<sup>[12,13]</sup> the precise interaction patterns and the role of each of them in NP transformation, degradation and recycling have yet to be unraveled.

The purpose of this paper is to get insight into the role of ferritin protein in the intracellular recycling and remediation of iron IONPs. After cellular uptake (mainly by cells of the mononuclear phagocytic system), NPs converge to intracellular compartments called lysosomes in which they endure the effects of acidic environment (pH 4.7), hydrolytic enzymes, and

a variety of proteins and lipids, collectively responsible for the degradation of NP's coating and core.<sup>[14]</sup> The loss of the protective layer on the metal or oxide surface, the chemical etching of the crystal itself and the affinity of metal chelators are intracellular events that govern the crystal disintegration, the release of metallic ions, and eventually the formation of metal complexes. Hence, the intracellular loss of NP integrity, observed for quantum dots,<sup>[15]</sup> silver NPs,<sup>[16]</sup> ZnO NPs,<sup>[17]</sup> or IONPs,<sup>[4c,18]</sup> has two major consequences: first, it alters the physical properties and functionalities of NPs and second, it may produce highly reactive and potentially harmful metal ions due to the cascade of chemical reactions to which particle components are exposed. Ferritin could be able to capture the free and potentially harmful iron species generated by the intracellular degradation of IONPs. It has been shown that lysosomal iron overload induce pro-oxidant conditions which trigger *de novo* ferritin synthesis or transfer of apoferritin by autophagy.<sup>[9b,19]</sup> Ferritins in lysosomes thus protect from iron overload and exert cytoprotective properties.<sup>[20]</sup> On the other hand, it may stimulate lysosomal stress and induce adverse effects.<sup>[21]</sup> Ferritin can be also degraded by proteases in lysosomes, thereby releasing iron.<sup>[22]</sup> The dynamics of endolysosomal iron pool thus serves as a rheostat of cellular iron flux which controls the lysosome stability.<sup>[9b]</sup> By monitoring the colloidal status and dissolution of IONPs in the presence of ferritin, we investigated for the first time the role of this protein in the behavior, aggregation and erosion of iron oxide nanocrystals. The capacity of ferritin cages to accommodate and store the degradation products of maghemite NPs was examined *in vitro* in a minimal medium mimicking the acidic environment of the lysosomes where NPs are physiologically confined and degraded. Moreover we questioned whether ferritin proteins could play an active role in the degradation of IONPs. The Nuclear Magnetic Resonance (NMR) relaxometric behavior as well as superparamagnetic and structural properties of IONPs was monitored over time in order to assess crystal degradation in the presence of different amounts of the protein and to follow the loss of MRI detectability. UV-visible spectroscopy and electron microscopy allowed assessing the transfer of iron from NPs to proteins. The colloidal status and transformations of both proteins and IONPs were monitored by small angle X-ray scattering (SAXS) and dynamic light scattering (DLS). The magnetic, colloidal, and structural follow-up of IONPs and proteins in lysosome-like medium confirmed the efficient remediation of iron ions generated by NPs within ferritins. The presence of ferritins, however, delayed the degradation of particles due to a complex colloidal behavior of the mixture in acidic medium. This study exemplifies the important implication of a particular intracellular protein in processes of metabolization of IONPs and in the regulation of their degradation.

## 2. Results and Discussion

### 2.1. Degradation of IONPs in Acidic Environment Mimicking the Lysosome pH

IONPs were previously shown to degrade in lysosomes<sup>[3b]</sup> as well as in a minimal medium mimicking the acidic pH of

lysosomes (pH 4.7) and containing citrate as iron chelator. The kinetics of degradation depended on NPs surface coating, size, shape, and architecture.<sup>[4c,e,18,23]</sup> Herein, we chose archetypical 7–8 nm superparamagnetic IONPs made by coprecipitation with different coating in order to evidence the role of ferritin in their degradation process (**Figure 1**). Their superparamagnetic properties, NMR relaxation behavior, colloidal stability, and morphology were first followed in an aqueous medium at pH 4.7 and  $20 \times 10^{-3}$  M citrate in the absence of ferritin. Electron Paramagnetic Resonance (EPR) was used to specifically detect the superparamagnetic IONPs as a function of time (**Figure 2A**). As the released iron ions have no or negligible EPR signal at room temperature in comparison to exchange-coupled iron in ferrimagnetic crystal lattice, the integration of the EPR absorption signal provides the measurement of the quantity of iron in the form of superparamagnetic particles (SP iron) remaining in the solution and thus an indirect determination of what is lost over time due to degradation of nanocrystals.<sup>[24]</sup> We observe an exponential decay of SP iron for citrate-coated IONPs, and a slower decay for dextran-coated IONPs (**Figure 2B**). Importantly, we observed no degradation in the absence of citrate at pH 4.7 or in the presence of citrate at pH 6.8 (data not shown).

To measure the efficacy of IONPs as MRI contrast agents and characterize their NMR magnetic properties over time, the longitudinal and transverse relaxation rates,  $R_1$  and  $R_2$ , were measured at Larmor frequencies close to those used in clinical scanners—20 MHz and 60 MHz—respectively corresponding to 0.5 T and 1.5 T magnetic fields. A deeper investigation was provided by Nuclear Magnetic Resonance Dispersion (NMRD) profile, which represents the longitudinal nuclear relaxation rate  $R_1$  as a function of the proton Larmor frequency on a large range of Larmor frequencies. NMRD measurement constitutes a valuable tool to characterize the magnetic properties of IONPs and their interactions with their local environment.<sup>[25]</sup> As shown in **Figure 2C–F**, at any fixed proton Larmor frequency,  $R_1$  and

$R_2$  decreased with time in acidic medium due to the loss of iron belonging to “efficient” particles that are able to boost proton relaxation. Indeed the relaxation of free iron ions is almost negligible when compared to the relaxation induced by the same amount of iron structured in IONPs. When  $R_1$  was normalized to its value at 0.015 MHz (**Figure 2D**), we observed that the high field inflection point of the NMRD profiles slightly shifted toward higher Larmor frequencies. This shift can be theoretically explained by a slight decrease of the minimal distance of approach of protons to the particles, reflecting the erosion of remaining particles.<sup>[25]</sup> It is important to note that the colloidal stability of citrate-coated IONPs was maintained all over their degradation in acidic medium. Indeed the size distribution deduced from DLS experiments was almost unmodified over days in acidic medium (**Figure 3B**). In contrast, the time-averaged intensity scattered at  $173^\circ$  (**Figure 3C**) progressively decreased in agreement with a diminution of the number of particles at constant NPs’ size. SAXS experiment was used to characterize both the form factor of IONPs and their colloidal state as a function of time. The evolution of SAXS patterns confirmed the DLS results (**Figure 3D**). All the curves obtained during the first 25 d could be well fitted with a sphere form factor with radius  $R = 2.3$  nm and log. normal polydispersity  $0.5 \leq PD \leq 0.6$ , without detectable aggregation in the available  $q$  range (**Figure S1**, Supporting Information). After 1 year no IONPs could be detected. The main effect of NP aging in acidic medium is a decrease of the scattered intensity at low and intermediate  $q$  ranges that should be related to IONPs dissolution. If we assume that IONPs keep their size and composition (i.e.,  $R = 2.3$  nm and molecular weight =  $150\,356$  g mol<sup>-1</sup>) during the degradation process, the time evolution of IONP concentration can be deduced from the relative intensity extrapolated to  $q \rightarrow 0$ , revealing a first-order kinetic with a characteristic time of 7.7 d, consistent with EPR and NMR relaxation results (**Figure 3E**).

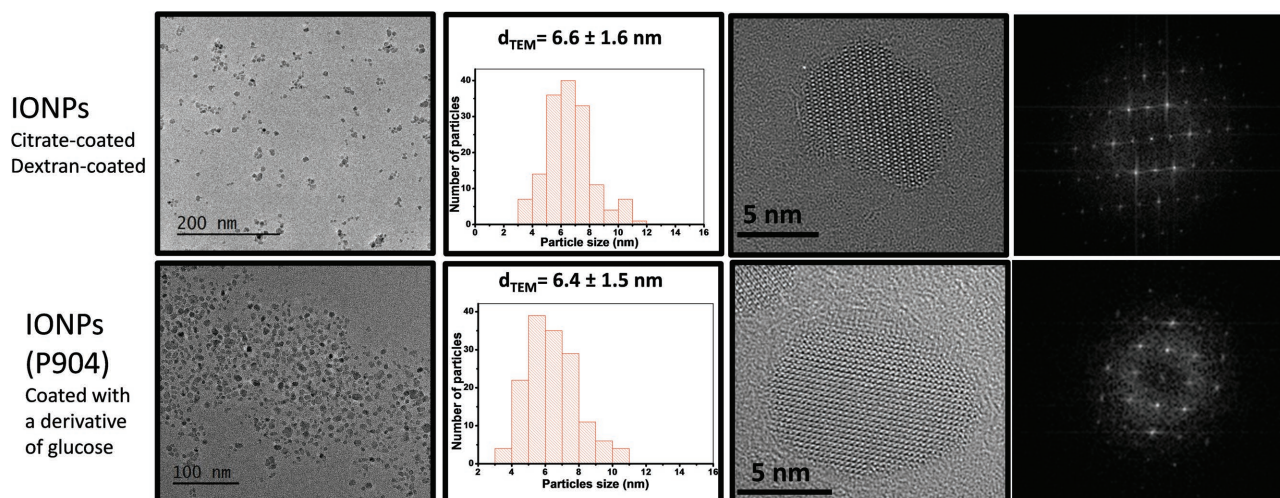


**Figure 1.** Description of IONPs used in the study. TEM images of citrate-coated IONPs (these IONPs were also coated with dextran) and IONPs coated with a derivative of glucose (P904) and corresponding TEM size distribution with a mean diameter of  $(6.6 \pm 1.6$  nm),  $(6.4 \pm 1.5$  nm), respectively. High-resolution images of IONPs and P904 and FFT of selected particles show monocrystalline inverse spinel structure oriented along the [112], [112], [001] zone axes, respectively.

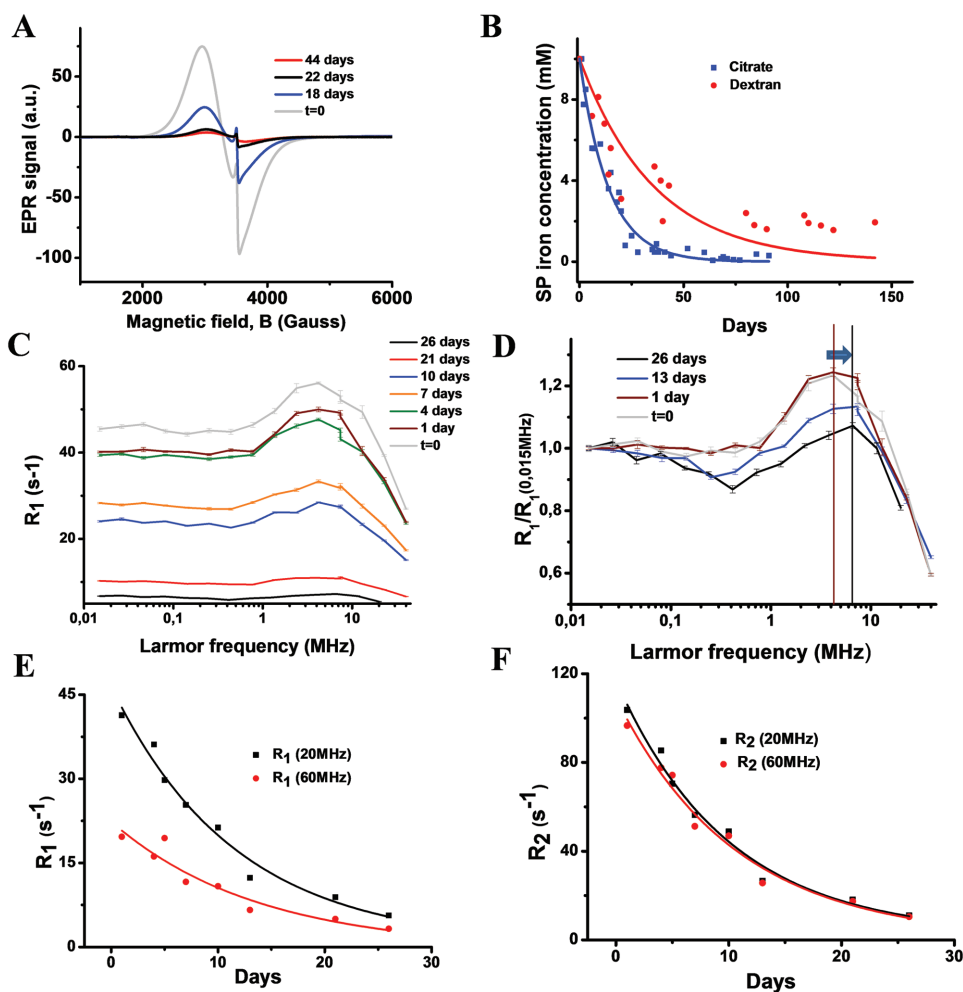


**Figure 2.** The evolution of magnetic properties of IONPs reveals their degradation in acidic medium. A) EPR signal as a function of time for citrate-coated IONPs. B) Integrated EPR signal measures the concentration of superparamagnetic iron in suspension. It decreases over time in acidic medium, faster for citrate-coated than for dextran-coated IONPs. C) NMRD profile of citrate-coated IONPs ( $1 \times 10^{-3}$  M iron concentration) at different time points in acidic medium. Note the incremental decrease of longitudinal relaxation rate  $R_1$ , regardless of the proton Larmor frequency. D) Normalized NMRD profile  $R_1/R_1(0.015 \text{ MHz})$  shows that the maximum of relaxation rate shifts toward higher frequency over time. E, F) Time evolution of the longitudinal and transverse relaxation rates of citrate-coated IONPs at proton Larmor frequencies of 20 and 60 MHz—corresponding to clinical MRI magnetic field of 0.5 and 1.5 T.

## 2.2. Signatures of Apoferritin and Metal-Filled Ferritin in Acidic Environment

Prior to the analysis of particles interactions with ApoF in acidic environment, we characterized the distinct behavior of ApoF and HoloF proteins in different environmental media. The SAXS curves of the commercial horse spleen protein stock solutions in water (pH 6.8) are plotted in **Figure 4A**. The SAXS pattern of ApoF shows a plateau for  $q \leq 0.02 \text{ \AA}^{-1}$  and two well-defined oscillations, at  $q = 8.7 \times 10^{-2}$  and  $1.50 \times 10^{-1} \text{ \AA}^{-1}$ . This curve fits the form factor of monodisperse vesicles with  $R_{\text{core}} = 3.2 \text{ nm}$  and a shell thickness  $t_s = 3.0 \text{ nm}$ , in line with the cage structure of ApoF. In contrast, the SAXS pattern of the HoloF stock solution presents a power-law decay for  $q \leq 0.03 \text{ \AA}^{-1}$  and slight oscillation at  $q = 1.65 \cdot 10^{-1} \text{ \AA}^{-1}$ . The form factor of full spheres with a radius of 3.3 nm and a log-normal polydispersity  $PD = 0.20$  fits the curve for  $q > 0.3 \text{ \AA}^{-1}$ , which is consistent with filled protein cages. However, the power-law

decay ( $I \propto q^{-0.85}$  for  $q \leq 0.03$ ) indicates the contribution of proteins' aggregates to the scattering.

To clarify the aggregation state, the ratio  $I(q)/P(q)$  was plotted in Figure S2 (Supporting Information), where  $P(q)$  is the form factor of the individual HoloF. The obtained low- $q$  data could be fitted by the Guinier expression and enable to estimate, neglecting the Virial effects between aggregates, the aggregation number ( $N_{\text{Agg.}} \approx 5$ ) and the radius of gyration ( $R_G = 15 \text{ nm}$ ) of the aggregates. This domain is followed by  $q^{-0.75}$  decay toward unity, suggesting that these small clusters have an elongated structure.

Importantly, the dispersion of ApoF and HoloF in the citrate buffer at pH 4.7 led to protein aggregation and to phase separation. As shown in Figure 4B, ApoF form large ramified aggregates characterized by a fractal dimension  $D_f \approx 1.4$  according to the power-law decay of  $I(q)$  observed for  $q \leq 0.03 \text{ \AA}^{-1}$ . At higher  $q$  values, the scattering pattern is well fitted by the form factor of ApoF. Although HoloF proteins were already aggregated in the stock solution, the

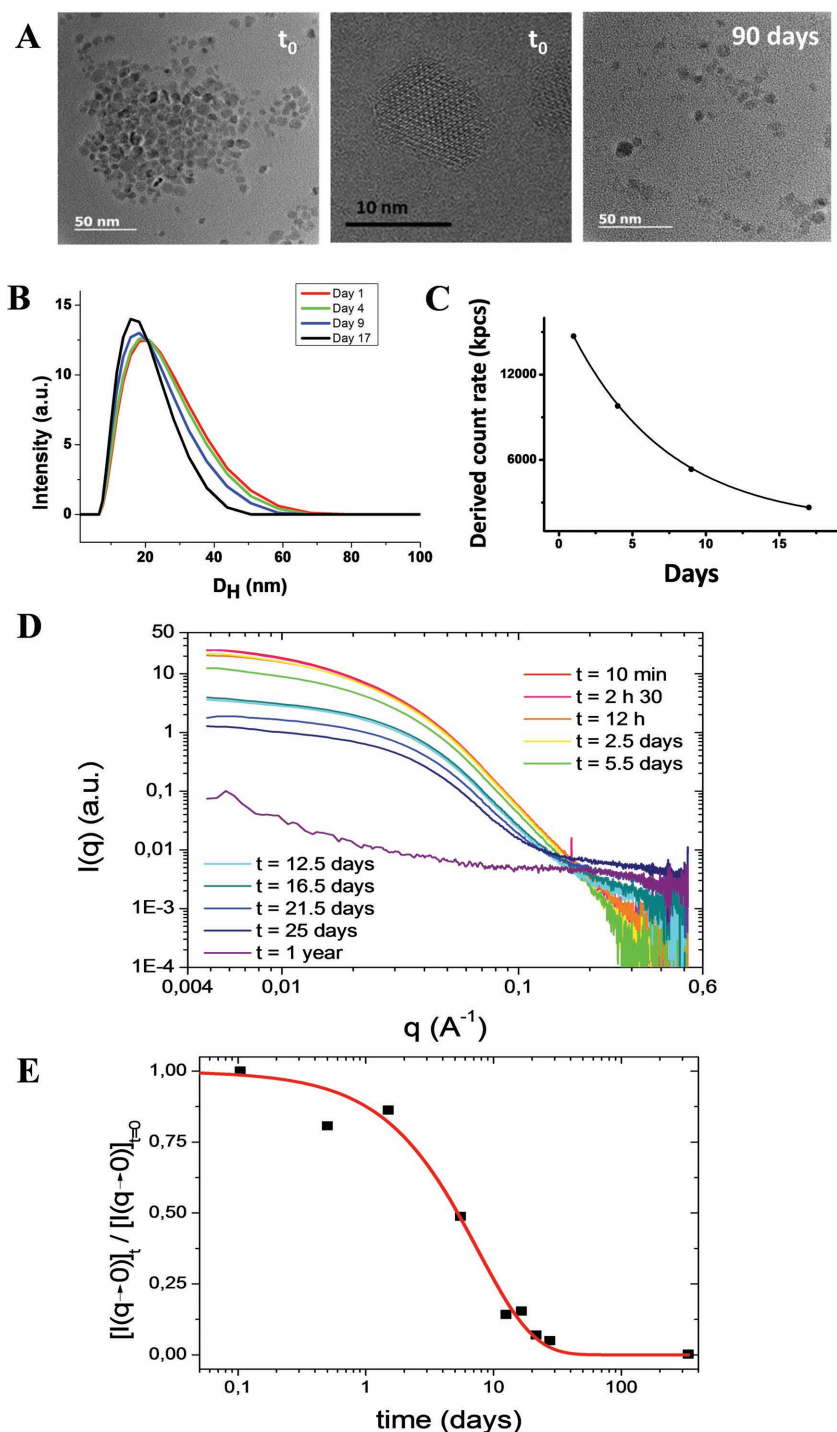


**Figure 3.** A) Representative TEM images of citrate-coated IONPs at different time points in acidic citrate buffer. B) Distribution of hydrodynamic sizes and C) derived count rate in light scattering experiments showing the growing scarcity of IONPs, while hydrodynamic size is only slightly decreased. D) SAXS curves of citrate-coated IONPs measured at different times after dispersion in the acidic citrate buffer ( $[\text{Fe}] = 10 \times 10^{-3}$  M). E) Time evolution of the SAXS normalized intensity  $I(q=0)_t / I(q=0)_{t=0}$ . The red line corresponds to the best adjustment of single exponential with a characteristic decay time of 7.7 days.

structure of aggregates was modified upon dispersion in acidic citrate buffer reaching a higher fractal dimension similar to the one of ApoF clusters. The low  $q$  part of the curve is still well fitted by the sphere form factor with  $R = 3.3$  nm and PD = 0.2.

Apart from different colloidal behaviors, ApoF can be distinguished from iron-filled HoloF by its UV-visible spectral signature. In comparison to ApoF spectrum, HoloF spectrum displays a shoulder band at 280 nm, which is due to the stored metal<sup>[26,27]</sup> and an intensity increase of the band at 220 nm (Figure 4C). HRTEM observations of commercial HoloF evidenced a size distribution with a mean diameter of  $5.8 \pm 0.8$  nm, mostly composed of hematite nanocrystals (Figure 3D).

Because the used IONPs are made of maghemite ( $\gamma\text{Fe}_2\text{O}_3$ ) and only comprise trivalent iron III, we first investigated if free iron III ions in solution could be transferred from salts to the protein core in acidic condition. The use of ApoF as nanoreactor was reported in ad-hoc conditions for NP synthesis,<sup>[28]</sup> but never in an acidic citrate medium. Moreover the transfer of iron ions to ApoF has been mostly described for divalent iron II and acidic media have been recognized as highly unfavorable for the ferritin binding of divalent metals except for  $\text{Fe}^{2+}$  and  $\text{Cu}^{2+}$  which remained unaffected by pH alteration.<sup>[29]</sup> Herein iron III salts were incubated with ApoF in acidic citrate medium for one day and subsequently dialyzed. UV-visible spectrum shows an intensity increase of the band at 220 nm, an evolution of the band at 280 nm and a charge-transfer band at 450 nm indicating a metal-protein bond (Figure 5A). These signals show a clear evolution toward the absorbance signal of commercial HoloF suggesting a filling of ApoF with iron. To confirm this result, the metal salt/ApoF mixtures were analyzed by HRTEM after an incubation time of two months (Figure 5B–F). For the iron salt-ApoF sample, transmission electron microscopy (TEM) images show the presence of crystalline NPs with a diameter of  $3.5 \pm 0.9$  nm (60% of the commercial HoloF size, Figure 5D), indicating a partial filling of the protein core. The structure of these nanocrystals was determined by analyzing the inter-reticular-distance ( $d_{\text{hkl}}$ ) distribution measured on many HRTEM images. As seen in figure 5C, some  $d_{\text{hkl}}$  exclusively correspond to the inverse spinel structure of iron oxide demonstrating that magnetite or maghemite nanocrystals formed inside protein shells. Nevertheless, due to the overlap of  $d_{\text{hkl}}$  between inverse spinel and hematite structures, hematite might have also grown inside the ferritin. Ferrihydrite, one of the phase frequently found in ferritin

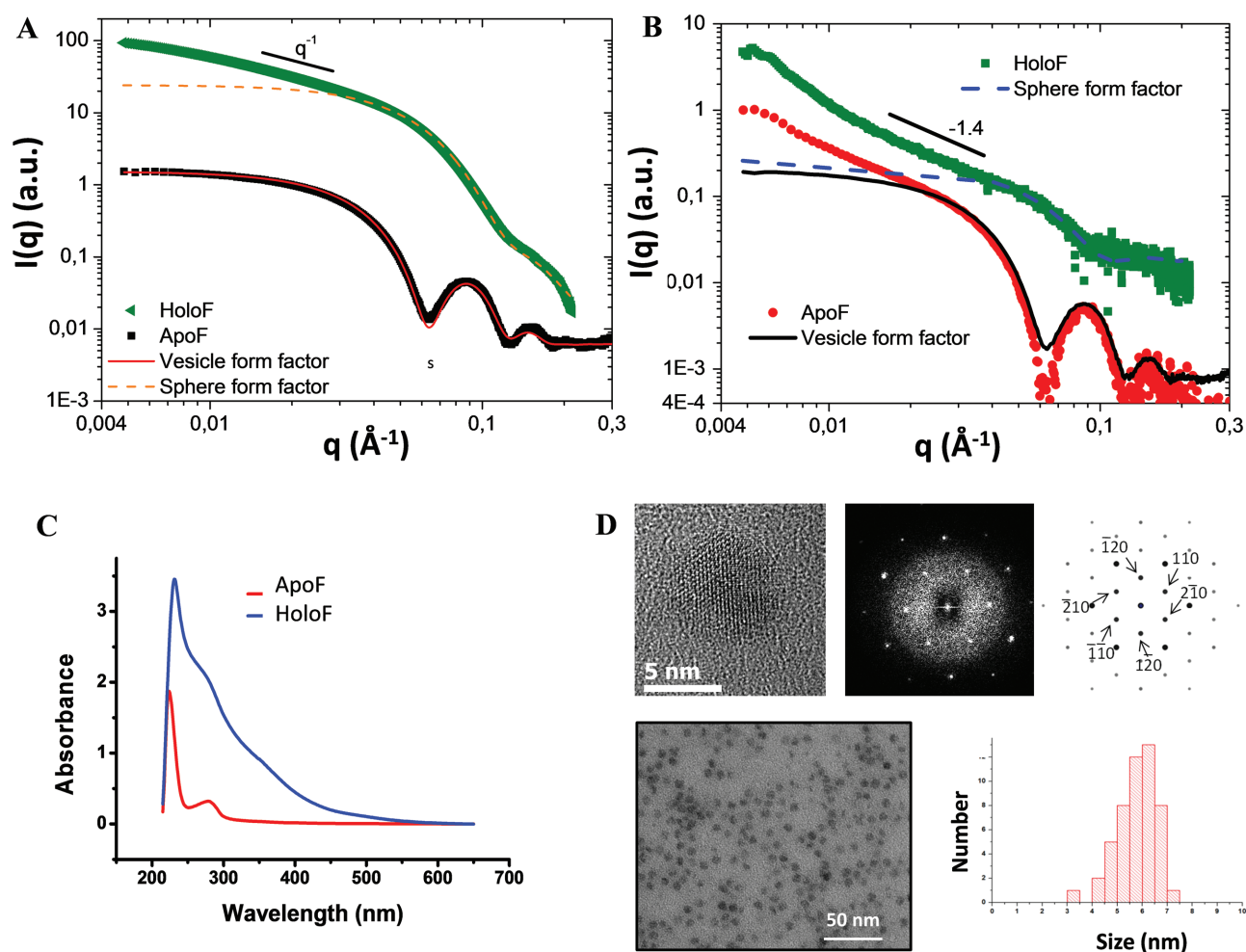


**Figure 4.** A) SAXS curves of Apoferritin and Holoferitin stock solution in water. The best fit corresponds to the form factor of plain spheres with radius  $R = 3.3$  nm and log-normal polydispersity  $PD = 0.2$  for HoloF (dashed orange line) and the form factor of monodisperse spherical vesicles with  $R_{\text{core}} = 3.2$  nm and shell thickness  $t_s = 3.0$  nm for ApoF (continuous red line). At low  $q$ , the power law as  $q^{-1}$  for HoloF indicates linear aggregates of proteins. B) SAXS curves obtained 1 h after dispersion of ApoF and HoloF in acidic citrate buffer. The lines correspond to the sphere form factor with  $R = 3.3$  nm and  $PD = 0.2$  (dashed blue line) and to the vesicle form factor with  $R_{\text{core}} = 3.2$  nm and shell thickness  $t_s = 3.0$  nm (continuous black line). The  $q^{-1.4}$  power-law decay at small  $q$  indicates the formation of loose fractal aggregates. C) UV-vis absorbance spectrum of ApoF and HoloF, showing the growth of an absorbance shoulder at 280 nm for iron-filled HoloF in comparison to iron-free ApoF. D) From left to right, HRTEM image of an HoloF nanocrystal, FFT of the HRTEM image showing the [001] zone axis of the hematite structure, simulated diffraction of hematite structure along the same zone axis. TEM image of HoloF and corresponding crystal size distribution (mean diameter  $5.8 \pm 0.8$  nm).

core,<sup>[7c,d]</sup> was not identified probably due to its poorly crystallized structure and sensitivity to the electron beam.<sup>[30]</sup> The nanostructures were analyzed by EDX in the STEM-HAADF mode, to check the colocalization of iron and of sulfur coming from the protein (Figure 5F). All these results confirm the uptake of iron III ions by ApoF and the mineralization of different iron oxides in the protein core.

### 2.3. Interactions of IONPs with Apoferritin: Aggregation State, NP Degradation, and Metal Transfer

Previous studies showing the presence of ferritins nearby NPs in organ slices suggest a potential transfer of iron relocating from NPs to ferritins.<sup>[3b,4e]</sup> We thus analyzed the evolution of ApoF interacting with IONPs in acidic citrate medium. During the 2 d of incubation at 37 °C, the absorbance signal

of ApoF evolved to that of the commercial HoloF, showing an incremental filling of ApoF with metals transferred from NPs (Figure 6A). The growth of the absorbance at 280 nm is summarized in Figure 6B for IONPs with different coatings (citrate, dextran, and hydrophilic derivative of glucose (P904)), indicating a partial and progressive filling of the protein, depending on the NPs. Consistently with the kinetics of degradation of IONPs (Figure 2B), the transfer of iron from citrate-coated NPs is faster than the one from dextran-coated NPs.

While ApoF is capable of recycling the byproducts of IONPs, it is unclear if it can catalyze per se the degradation of IONPs. Due to its intrinsic capacity to sequester iron, ApoF could shift the equilibrium in the direction of NP dissolution. Therefore we analyzed the degradation of NPs in acidic citrate medium in the presence of different ratios of ApoF with respect to the total iron concentration,  $\zeta = 1, 2$  or 4. For  $\zeta = 1$ ,

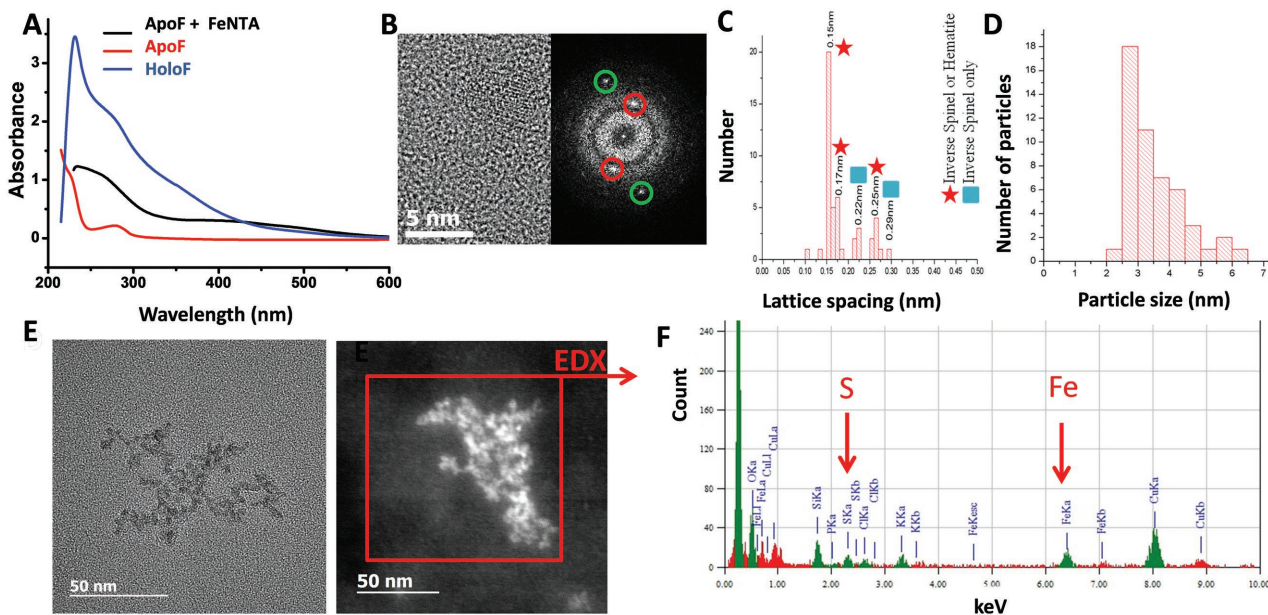


**Figure 5.** Signature of apoferritin filling with iron from metal salt, FeNTA. A) UV-vis spectrum of ApoF incubated with FeNTA for 22 h in acidic medium in comparison to ApoF alone and HoloF. Note the growth of the absorbance shoulder at 280 nm indicating the filling of the protein cage. B) HRTEM of ApoF incubated with FeNTA shows a crystalline structure with a diffraction spectrum displaying two systems of lattice fringes with lattice spacing of 0.22 and 0.29 nm characteristic of the inverse spinel structure of magnetite or maghemite (planes (113) and (440), zone axis [112]). C) Histogram of inter-reticular distance observed in ferritin nanocrystals, demonstrating the presence of the inverse spinel structure and possibly the presence of the hematite structures. D) Distribution of crystal sizes (mean diameter  $3.5 \pm 0.9$  nm) suggesting a partial filling of the protein cage, in line with UV-Vis spectrum. E) HRTEM and STEM-HAADF images of a ferritin particle aggregate and F) EDX analysis of the red area depicted in (F), indicated characteristic lines of iron and sulfur.

the number of iron atoms available in particles is equal to the maximal number of iron that can be stored in ApoF (i.e., 4500 iron atoms per ApoF protein). For  $\zeta = 2$  ( $\zeta = 4$ ), we have two (respectively, four) proteins for 4500 available metal atoms. Surprisingly, the kinetics of NP degradation, evaluated by EPR (Figure 7A), was slowed down by the presence of ApoF, regardless of particle coating (citrate or dextran). The larger the excess of proteins, the longer the characteristic time of NP degradation. The NMR relaxation measurements corroborate this finding with a slower diminution of the longitudinal relaxation rate  $R_1$  in the presence of ApoF (Figure 7C). Importantly, by fitting the NMRD profiles using

EPR determination of superparamagnetic iron concentration, one can deduce the minimal distance of approach between the citrate-coated IONPs and water protons in the sample. While this distance slightly decreases in the absence of ApoF ( $\zeta = 0$ ) indicating the degradation of IONPs, it increases with the excess of ApoF during the first days in acidic medium and then decreases again (Figure 7B). Consistently, the transverse relaxation rate  $R_2$  shows similar variations over time. These results can be explained by the transient aggregation of NPs with proteins or by the formation of a protein corona around the NPs, both processes being susceptible to delay IONP dissolution. This aggregation is nevertheless followed by the

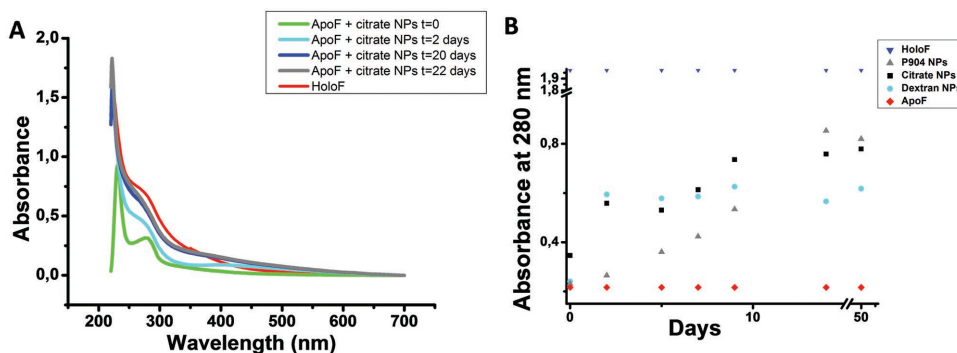


**Figure 6.** Follow-up of iron transfer from NPs to apoferritin proteins. In all experiments, the ApoF/NPs ratio is  $\zeta = 1$ . A) UV-vis spectra of ApoF incubated with citrate-coated IONPs in acidic medium for different times in comparison to ApoF and HoloF. The growth of absorbance shoulder at 280 nm indicates metal filling of the protein. B) Kinetic of metal transfer in proteins measured by the evolution of the 280 nm absorbance of ApoF incubated with IONPs with different coating (citrate, dextran, and hydrophilic derivative of glucose (P904)). Note the partial filling of proteins in comparison to HoloF.

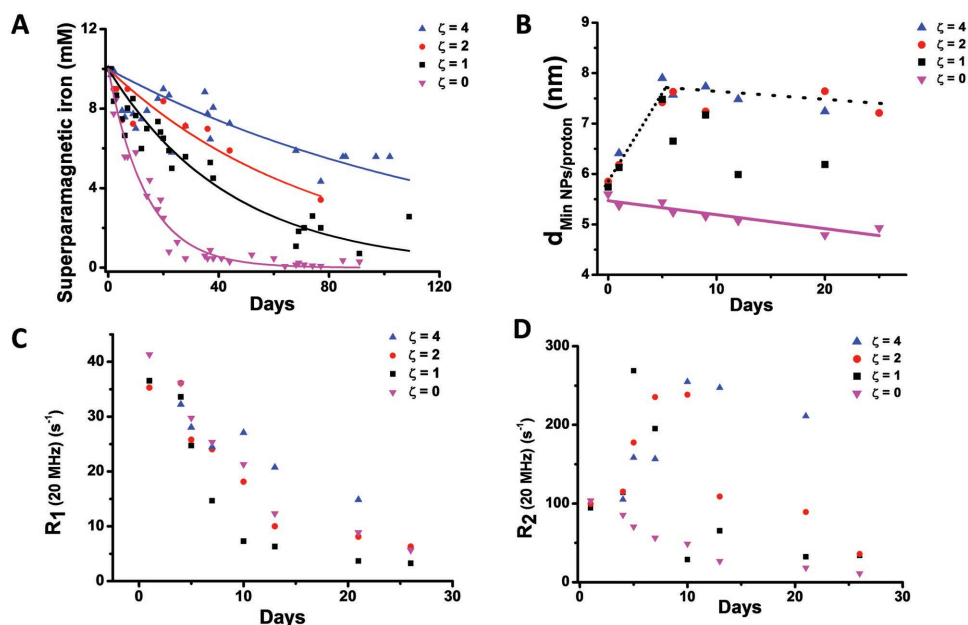


**Figure 7.** Degradation kinetics of citrate-coated IONPs in the presence of different ratios  $\zeta$  of ApoF in acidic medium. A) Time evolution of the superparamagnetic iron derived from EPR measurements. The higher the ratio of ApoF, the slower the kinetics of NP degradation. B) Minimal distance of approach between IONPs and water protons deduced from NMRD profiles. This distance continuously diminishes in the absence of ApoF, but increases first and then diminishes in the presence of ApoF. The transient distance increase is due to protein–particle aggregation, while its diminution results from IONPs degradation. Time evolution of the C) longitudinal and D) transverse relaxation rates at 20 MHz for different ratios  $\zeta$  of ApoF. The diminution of  $R_1$  results from the interplay of IONPs degradation and protein-induced aggregation.  $R_2$  first increases due to aggregation and then diminishes due to degradation.

delayed degradation of NPs, which tends to diminish the minimal distance of approach of water protons.

To deeper investigate the interactions of NPs with proteins and characterize the colloidal dynamics of the mixture for different protein ratios, SAXS experiments were carried out. Ten minutes after mixing, all protein-NPs samples were homogenous but their SAXS spectrum differed from that of IONPs alone ( $\zeta = 0$ ) by the presence of “extra scattering” at low and high  $q$  range. At low  $q$  range, the power law decay,  $I \propto q^{-1.6}$ , indicates the presence of aggregates of IONPs with proteins and the high  $q$  range reflects the contribution of ApoF form factor, notably at  $\zeta = 4$  when the form factor oscillations are visible.

As the dispersion of IONPs with ApoF led to phase separation in the studied range of protein ratio, we characterized the supernatant at different aging times after mixing. The SAXS curves corresponding to supernatant at  $\zeta = 1$  and 4 for the different stages of the degradation process are shown in **Figure 8B,C**. In the protein-free acidic medium ( $\zeta = 0$ ), the intensity scattered at  $q = 0.02 \text{ \AA}^{-1}$  decays exponentially due to the degradation of IONPs. On the contrary, the scattered intensity shows a nonmonotonous evolution in the presence of ApoF (**Figure 7A**). Actually, a three-stage kinetics appears for  $\zeta \geq 1$ .

The first stage takes place during the first two days and corresponds to a decrease of the normalized intensities until a minimum due to the destabilization of ApoF/IONPs mixture. A complete phase separation rapidly occurs at  $\zeta = 1$ , segregating particles and proteins in the dense phase and a highly diluted solution of aggregated ApoF in the supernatant. When enhancing the protein ratio  $\zeta$  from 1 to 4, the destabilization is less marked and slower.

The evolution of the supernatant SAXS pattern at  $\zeta = 4$  indicates that more and more IONPs are associated and stabilized by ApoF in the supernatant.

The second step, characterized by an increase of the scattering intensity in the supernatant, reveals a redispersion process of both proteins and NPs from the dense phase to the supernatant. This redispersion can reflect a partial degradation of IONPs in the dense phase. As NP degradation occurs, the number of NPs and the total area at NPs’ interfaces decrease. As a consequence the apparent protein number per particle increases leading to a spontaneous restabilization of NPs/protein complexes. Consistently, this redispersion sets on faster when increasing the protein ratio, confirming the crucial role of ApoF protein corona in the restabilization process.

In the final step, the suspension becomes homogeneous and the scattering intensity decreases again due to IONPs degradation.

Overall, we can conclude that the formation of NPs/protein aggregates and of ApoF corona around NPs initially restricts the access of the citrate to the NPs surface and slows down the kinetics of NPs degradation. The effective transfer of metal ions into ApoF cavity did not accelerate NP degradation in acidic citrate medium, which rather results from the interplay between colloidal stability governed by NP/protein interactions and access of iron chelators to the NP surface. This statement was definitely established by complementary experiment in which NPs and ApoF were separated by a dialysis membrane permeable to small molecules such as citrate, iron ions or citrate-iron complexes (**Figure 9A**). Indeed when close interactions between NPs and ApoF were abolished,

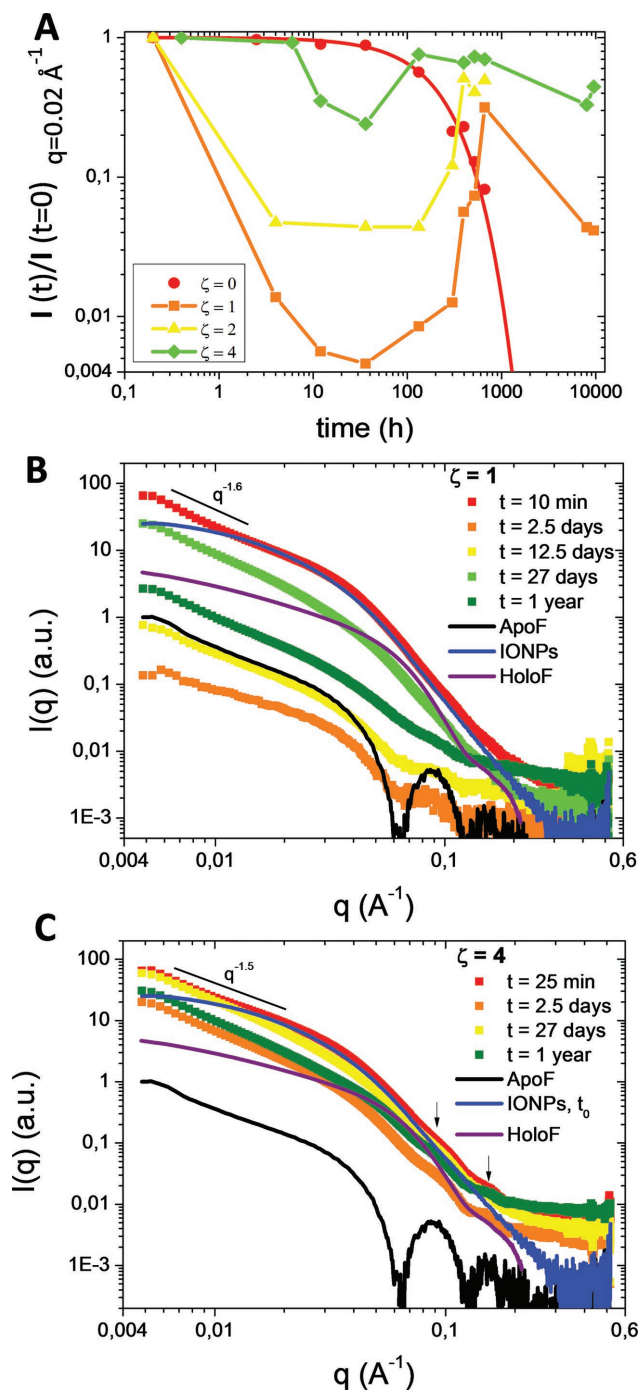


**Figure 8.** A) Time evolution of the SAXS intensity measured at  $q = 0.02 \text{ \AA}^{-1}$  and normalized to the intensity at  $t = 0$  for the supernatant of citrate-coated IONPs in the presence of different protein ratio  $\zeta$  of ApoF as indicated in the inset. The red line corresponds to the best adjustment of single exponential with characteristic degradation time of 7.7 d. The other lines are guides for the eye. SAXS curves of ApoF/IONPs mixtures (supernatant) at different time points in acidic citrate medium and different protein ratios  $\zeta =$  B) 1 and C) 4. The continuous lines correspond to the SAXS pattern of ApoF (black curve), HoloF (violet curve), and IONPs diluted in the citrate buffer 1 h after dispersion.

we observed similar degradation kinetics in the presence and absence of ApoF, confirming the importance of protein/NP contact in the regulation of degradation.

The question remained whether and to what extent ApoF could eventually favor the degradation of IONPs by direct chelation of iron on the surface of the particles, competing with citrate or other chelating agents. We thus performed degradation experiments in citrate-free acetate buffer (acetate  $40 \times 10^{-3} \text{ M}$ , pH 4.7) in which IONPs remained quasi-intact for long period of time in the absence of ApoF. As shown in Figure 9B, IONPs started to degrade in the presence of ApoF ( $\zeta = 1$ ), with a faster kinetics for the citrate-coated IONPs in comparison to dextran-coated NPs (Figure 9B). This is consistent with a direct role of ApoF protein in the complexation of iron coming from particles. The access of ApoF to iron at the surface of particles is less easy in case of dextran coating, known to be an antifouling coating, compared to citrate-coating. We thus conclude that ApoF per se has the ability to induce IONP degradation and directly accommodate their residues. Figure 9C shows the different degradation kinetics for citrate-coated NPs in acetate buffer or citrate buffer. As described previously, the degradation of IONPs in citrate buffer is slowed down in the presence of ApoF due to the formation of an ApoF corona around the NPs. This ApoF shield restricts the access of citrate to the NPs and thus slow down the degradation of the NPs. In the citrate buffer there are two degradation mechanisms: the dissolution of the NPs by the citrate ligand (fast) and the erosion of the NPs by the ApoF (slow). When an excess of ApoF is added to the NPs ( $\zeta = 4$ ) in the citrate buffer the evolution of the superparamagnetic iron concentration tend to the evolution in the acetate buffer meaning a progressive and almost total covering of ApoF around the IONPs (Figure 9C). Thus the ApoF protects the IONPs from the citrate ligand and the degradation of the NPs is governed by the sole effect of ApoF proteins.

#### 2.4. Significance for In Vivo Remediation of IONPs

In previous studies, high-resolution observations of organs excised from treated animals provided information on the ultrastructure of lysosomes in macrophages located within different tissues (spleen, liver,<sup>[4a,c,11b]</sup> or inflammatory sites such as adipose tissue<sup>[31]</sup> or atherosclerotic plaques<sup>[11a]</sup>) and pointed out the ubiquitous presence of HoloF nearby or within IONP-rich zones. In addition, the local lysosomal degradation of IONPs has been empirically demonstrated<sup>[3b,4b]</sup> and the transfer of  $^{59}\text{Fe}$  from IONPs to the hemoglobin of rats<sup>[5a]</sup> and mice<sup>[5b]</sup> was established. Here we first showed that ApoF could accommodate in its cavity relevant quantities of iron III after incubation with metal salts at the acidic, lysosome-like pH, but also iron ions released from IONPs in the course of their degradation in the acidic citrate medium. ApoF has been proposed as bioreactor for the encapsulation of various metallic compounds and drugs by disassembly/reassembly of the protein shell under specific conditions. However its capacity to store iron III ions released from NPs under physiologically relevant conditions was never investigated. Our finding suggests the capacity of ferritin to store iron ions released by IONPs in lysosomes and consequently avoid harmful reactions related to free metal ions, providing protection against oxidative stress.

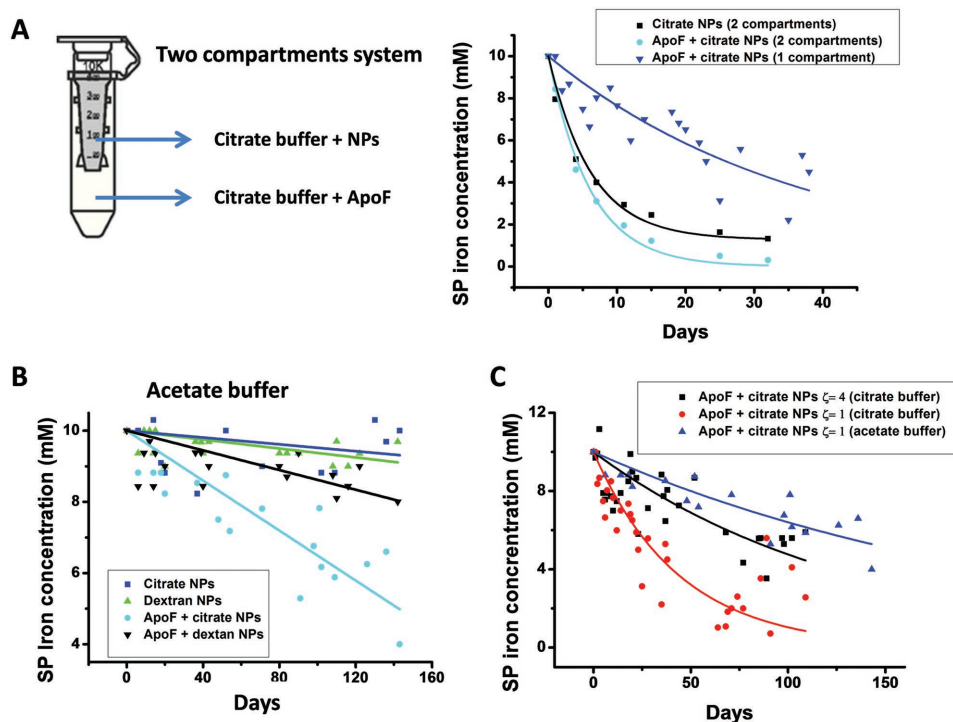


**Figure 9.** A) Comparison of the degradation kinetics of citrate-coated IONPs in acidic citrate medium in cases NPs and ApoF are mixed with  $\zeta = 1$  in a single compartment or are separated by a dialysis membrane in two compartments as illustrated in the scheme. ApoF delays the degradation of IONPs only if contact with NPs is granted. B) Degradation of citrate-coated and dextran-coated IONPs in acidic acetate medium ( $\zeta = 1$ ) showing that ApoF by itself is able to trigger the dissolution of citrate-coated NPs and to a lesser extent of dextran-coated NPs. C) Comparison of the degradation of citrate-coated IONPs in acidic citrate and acetate medium for  $\zeta = 1$  and 4.

The role of metal chelating agents as intermediates for metal transfer and recycling in ferritin requires further investigation into more realistic and more complete lysosomal media. Particularly ferritins can be degraded by proteases in lysosomes and partially lose their ferroxidase activity. Note the ferroxidase activity of ferritin, provided by ferritin H subunit, is not mandatory for the recycling and nucleation of iron ions coming from maghemite NPs which comprise iron in its already oxidized state. This point has been confirmed recently in a tissue model consisting of stem cell spheroid labeled with maghemite NPs.<sup>[3b]</sup> IONPs were shown to degrade into endolysosomal compartments of stem cells, while ferritin L gene expression responsible for iron binding and nucleation was overexpressed, but not ferritin H. Nevertheless, we observed that, in the absence of more potent iron chelating agent, ApoF per se could trigger the degradation of IONPs and accommodate iron III ions. In the presence of citrate ions, which by itself induce the degradation of particles in acidic conditions, the dissolution of IONPs was delayed and not accelerated by the presence of ApoF. The unexpected delay in IONPs degradation, observed after increasing the ratio of apoferritin in the acidic medium, can be explained by a complex and dynamic colloidal behavior within the mixture as shown by SAXS investigations. When mixed with ApoF at increasing ratios, IONPs are destabilized and assemble with proteins to form loose aggregates. Although IONPs dissolution is delayed by aggregation owing to restricted access of ApoF and citrate ions to the NP surface, the aggregates tend to dissociate at longer times which eventually results in the

dissolution of IONPs and the transfer of iron into the protein cage. This dynamic evolution of the NP/protein complexes is confirmed by NMR relaxation measurements, which revealed both the rarefaction of relaxation rates) and the nonmonotonous variation of the proton accessibility to the magnetic cores, restricted by the shield of aggregated proteins. Remarkably, the different nanostructurations of ferritin proteins were also observed in tissue samples, particularly within lysosomes.<sup>[4a,c]</sup> For example, HoloF are frequently assembled in large separated structures or are present as loose aggregates surrounding the NPs. In view of the present results, the biogenesis, recruitment and spatial distribution of ferritin proteins around administered NPs could be a step in the cell's strategy to modulate IONPs degradation and iron transfer, and regulate the availability of free and reactive metal ions in lysosomes.

### 3. Conclusion

In conclusion, this study relied on different complementary methods to monitor the degradation of metal oxide NPs, the loss of their magnetic and functionally relevant properties, their morphological change, and aggregation status in the presence of ferritin proteins. Our results demonstrate, at the nanoscale, the transfer of iron from IONPs to endogenous ferritin proteins in the acidic conditions of lysosomes and highlight the role of ferritin in the remediation of

NP-released metal ions. The relative spatial structuration of NPs with ferritins is shown to have a crucial effect on their degradation and recycling processes.

## 4. Experimental Section

**Nanoparticles:** All NPs used in this study were synthesized by coprecipitation method according to Massart's procedure.<sup>[32]</sup> IONPs consisted of a magnetic (magnetite) core obtained by coprecipitation of ferrous and ferric ions and fully oxidized to maghemite ( $\gamma\text{Fe}_2\text{O}_3$ ). IONPs were covered with citrate (citrate-coated IONPs), carboxymethyl dextran (dextran-coated IONPs), or a hydrophilic aminoalcohol derivative of glucose grafted by phosphonate groups on the surface of NPs (P904, developed by Guerbet SA for MRI imaging of inflammation process).<sup>[31]</sup> The suspensions were stable in water in a pH range of 3–8 owing to electrostatic stabilization (negatively charged citrate-coating) or both steric and electrostatic repulsions (dextran and derivative of glucose).<sup>[33]</sup> The size distributions of the NPs were determined by TEM. The hydrodynamic diameter was determined by DLS in water and was in the range of 20–40 nm. Detailed NPs specifications are reported in Figure 1.

**TEM:** HRTEM imaging and EDX spectroscopy were performed on a JEOL ARM 200 F microscope, equipped with a CEOS aberration corrector, a cold field emission gun and a JEOL EDX diode, operated at 200 kV.<sup>[34]</sup>

**Lysosome-Like Buffer:** The medium used to mimic the acidic environment of the lysosomes, as described by Arbab et al.<sup>[18b)]</sup> consisted of  $20 \times 10^{-3}$  M citric acid at pH 4.7. The acidic citrate buffer was prepared by mixing  $10 \times 10^{-3}$  M of citric acid ( $\text{C}_6\text{H}_8\text{O}_7$  Fluka, >99.5%) and  $10 \times 10^{-3}$  M of sodium citrate tribasic ( $\text{C}_6\text{H}_7\text{Na}_3\text{O}_7 \cdot 2\text{H}_2\text{O}$ , Fluka >99%) in 250 mL of purified water.

**Metal Transfer to ApoF: Filling of ApoF with Metal Complexes Salts:** A  $0.05 \times 10^{-3}$  M solution of ApoF (apoferritin from equine spleen, Sigma) was incubated at 37 °C for 1 d with an excess of iron(III) nitrilotriacetate complex (FeNTA,  $5 \times 10^{-3}$  M) in the acidic citrate buffer and the mixture was dialyzed (Dialysis membrane 50 kD, Spectrum Labs) to remove the excess of iron salt.

**Filling ApoF with IONPs:** The IONPs were incubated with ApoF in the acidic citrate buffer for different times, the final concentrations being  $0.12 \times 10^{-3}$  M of NPs and  $0.5 \times 10^{-6}$  M of ApoF.

**UV-Visible Spectroscopy:** Absorption measurements were performed at  $(37 \pm 0.5)$  °C on a Cary 4000 UV/Vis/NIR spectrophotometer equipped with a thermostated cell carrier. The signal of nondegraded NPs was subtracted to remove the diffusion signal related to NPs.

**In Vitro NP Degradation Procedure:** NPs were incubated at 37 °C in the dark with and without ApoF in the acidic citrate or acetate buffer at  $20 \times 10^{-3}$  and  $40 \times 10^{-3}$  M respectively with a final iron concentration of  $10 \times 10^{-3}$  M. ApoF was used at different ratios,  $\zeta = 0, 1, 2, \text{ or } 4$ . Each ApoF could accommodate up to 4500 iron atoms. For  $\zeta = 1$ , there were 4500 atoms of iron available for one apoF ( $10 \times 10^{-3}$  M iron,  $2.2 \times 10^{-6}$  M ApoF) and for  $\zeta = 4$ , 4500 atoms of iron for four apoF ( $10 \times 10^{-3}$  M iron,  $8.8 \times 10^{-6}$  M ApoF). Amicon filters 10K were used for the experiment where the NPs were separated from the ApoF (two compartments). In the first compartment, the NPs (iron concentration =  $10 \times 10^{-3}$  M) were incubated in the citrate buffer at  $20 \times 10^{-3}$  M and the second compartment contained the citrate buffer at  $20 \times 10^{-3}$  M without or

with apoF ( $\zeta = 1$ ). The suspensions were characterized by physical methods described below.

**NMRD:** The frequency dependence of the longitudinal  $^1\text{H}$  relaxation rate,  $R_1 = 1/T_1$ , was recorded in the suspension over the frequency range of 0.015–40 MHz using a Spinmaster FFC-2000 fast-field cycling NMR relaxometer (Stelar SRL, Mede, Italy). The temperature of the samples was maintained at 37 °C using a thermostated airflow system. All of the  $^1\text{H}$  magnetization recovery curves were monoexponential within experimental error, and the random errors in fitting  $T_1$  were always less than 2%.  $R_1$  and  $R_2 (= 1/T_2)$  were also measured using the inversion recovery and CPMG pulse sequence with an interecho time of 1 ms, respectively, on a 20 MHz and on a 60 MHz Bruker Minispec. All measurements were performed in samples with iron concentration of  $1 \times 10^{-3}$  M, prepared by aqueous extemporaneous 10-times dilutions of the suspensions in acidic citrate medium taken at different incubation times.

**EPR:** EPR was performed with an E500 EPR spectrometer operating at X band frequencies (9.5 GHz). The first derivative of the absorption  $dW(B)/dB$  was recorded as a function of the applied field  $B$  in the range 0–10 kGauss with a microwave power of 1 mW. The signal was collected for small volumes (2  $\mu\text{L}$ ) of IONP suspensions, at iron concentration of  $10 \times 10^{-3}$  M, inserted in capillary Wiretrol II 1–5  $\mu\text{L}$  (VWR, France). The area of the EPR absorption curve, calculated by a double integration of the spectrum  $dW(B)/dB$ , was proportional to the amount of superparamagnetic IONPs in the sample. An absolute calibration was performed using suspensions of initial IONPs at different iron concentrations, quantified by ICP-MS. It was checked that paramagnetic iron species that could be released in the acidic medium were not contributing to the EPR signal at room temperature.

**DLS:** DLS measurements were carried out at 25 °C on a Zeta Sizer Nano ZS (Malvern Instruments) equipped with a 5.0 mW He-Ne laser operating at 632.8 nm and an Avalanche photodiode detector. The time-averaged intensity of scattered light at 173° (derived count rate) was used to quantify the number of scattering NPs in course of their degradation. It was also verified that for the native nondegraded NPs, the time-averaged intensity of scattered light was proportional to the iron concentration. The dispersions were never filtered before measurements.

**SAXS:** SAXS experiments were performed at 25 °C with samples ( $[\text{Fe}] = 0 \text{ or } 10 \times 10^{-3}$  M,  $[\text{ApoF}] = 0, 2.2 \times 10^{-6}, 4.4 \times 10^{-6}, \text{ or } 8.8 \times 10^{-6}$  M in acidic citrate medium; or  $[\text{ApoF}] = 8.8 \times 10^{-6}$  M or  $[\text{HoloF}] = 8.8 \times 10^{-6}$  M in water) placed in sealed quartz capillaries on two synchrotron beamlines:

- SWING beamline (SOLEIL synchrotron at Saint-Aubin, France) with a configuration  $D = 2.1$  m and  $\lambda = 1$  Å to get a  $q$ -range from  $4.8 \times 10^{-3}$  to  $0.52$  Å $^{-1}$ .
- BL11-NCD beamline (ALBA synchrotron at Barcelona, Spain) with the following configuration:  $D = 6.1$  m and  $\lambda = 1$  Å to get a  $q$ -range from  $4.8 \times 10^{-3}$  to  $0.21$  Å $^{-1}$ .

## Supporting Information

Supporting Information is available from the Wiley Online Library or from the author.

## Acknowledgements

This work was supported by ANR (Agence Nationale de la Recherche) and CGI (Commissariat à l'Investissement d'Avenir) through Labex SEAM (Science and Engineering for Advanced Materials and devices; ANR 11 LABX 086, ANR 11 IDEX 05 02), by the CNRS (Defi Nano) and DIM C'Nano Ile de France. The authors are grateful to Y. Frappart and S. Lajnef for EPR experiments. The authors are grateful to Guerbet company for providing with P904 IONPs. The authors acknowledge synchrotron SOLEIL (SWING, SOLEIL, Saint-Aubin, France) and synchrotron ALBA (Barcelona, Spain) for SAXS beam time allocation and Thomas Bizien and Marc Malfois for their assistance.

- [1] H. Liu, J. Zhang, X. Chen, X.-S. Du, J.-L. Zhang, G. Liu, W.-G. Zhang, *Nanoscale* **2016**, *8*, 7808.
- [2] H. Arami, A. Khandhar, D. Liggitt, K. M. Krishnan, *Chem. Soc. Rev.* **2015**, *44*, 8576.
- [3] a) N. Feliu, D. Docter, M. Heine, P. del Pino, S. Ashraf, J. Kolosnjaj-Tabi, P. Macchiariini, P. Nielsen, D. Alloyeau, F. Gazeau, R. H. Stauber, W. J. Parak, *Chem. Soc. Rev.* **2016**, *45*, 2440; b) F. Mazuel, A. Espinosa, N. Luciani, M. Refay, R. Le Borgne, L. Motte, K. Desboeufs, A. Michel, T. Pellegrino, Y. Lalatonne, C. Wilhelm, *ACS Nano* **2016**, *10*, 7627.
- [4] a) M. Levy, N. Luciani, D. Alloyeau, D. Elgrabli, V. Deveaux, C. Pechoux, S. Chat, G. Wang, N. Vats, F. Gendron, C. Factor, S. Lotersztajn, A. Luciani, C. Wilhelm, F. Gazeau, *Biomaterials* **2011**, *32*, 3988; b) J. Kolosnjaj-Tabi, Y. Javed, L. Lartigue, J. Volatron, D. Elgrabli, I. Marangon, G. Pugliese, B. Caron, A. Figuerola, N. Luciani, T. Pellegrino, D. Alloyeau, F. Gazeau, *ACS Nano* **2015**, *9*, 7925; c) L. Lartigue, D. Alloyeau, J. Kolosnjaj-Tabi, Y. Javed, P. Guardia, A. Riedinger, C. Pechoux, T. Pellegrino, C. Wilhelm, F. Gazeau, *ACS Nano* **2013**, *7*, 3939; d) A. Ruiz, Y. Hernandez, C. Cabal, E. Gonzalez, S. Veintemillas-Verdaguer, E. Martinez, M. P. Morales, *Nanoscale* **2013**, *5*, 11400; e) A. Ruiz, L. Gutierrez, P. R. Caceres-Velez, D. Santos, S. B. Chaves, M. L. Fascinelli, M. P. Garcia, R. B. Azevedo, M. P. Morales, *Nanoscale* **2015**, *7*, 16321; f) R. Mejias, L. Gutiérrez, G. Salas, S. Pérez-Yagüe, T. M. Zotes, F. J. Lázaro, M. P. Morales, D. F. Barber, *J. Controlled Release* **2013**, *171*, 225; g) J. Kolosnjaj-Tabi, L. Lartigue, Y. Javed, N. Luciani, T. Pellegrino, C. Wilhelm, D. Alloyeau, F. Gazeau, *Nano Today* **2016**, *11*, 280.
- [5] a) R. Weissleder, D. D. Stark, B. L. Engelstad, B. R. Bacon, C. C. Compton, D. L. White, P. Jacobs, J. Lewis, *AJR, Am. J. Roentgenol.* **1989**, *152*, 167; b) D. Pouliquen, J. J. Le Jeune, R. Perdrisot, A. Ermias, P. Jallet, *Magn. Reson. Imaging* **1991**, *9*, 275; c) B. Freund, U. I. Tromsdorf, O. T. Bruns, M. Heine, A. Giemsa, A. Bartelt, S. C. Salmen, N. Raabe, J. Heeren, H. Ittrich, R. Reimer, H. Hohenberg, U. Schumacher, H. Weller, P. Nielsen, *ACS Nano* **2012**, *6*, 7318; d) E. Okon, D. Pouliquen, P. Okon, Z. V. Kovaleva, T. P. Stepanova, S. G. Lavit, B. N. Kudryavtsev, P. Jallet, *Lab. Invest.* **1994**, *71*, 895.
- [6] a) E. Pawelczyk, A. S. Arbab, S. Pandit, E. Hu, J. A. Frank, *NMR Biomed.* **2006**, *19*, 581; b) R. Schafer, R. Kehlback, J. Wiskirchen, R. Bantleon, J. Pintaske, B. R. Brehm, A. Gerber, H. Wolburg, C. D. Claussen, H. Northoff, *Radiology* **2007**, *244*, 514.
- [7] a) E. C. Theil, *Curr. Opin. Chem. Biol.* **2011**, *15*, 304; b) R. K. Watt, R. J. Hilton, D. M. Graff, *Biochim. Biophys. Acta, Gen. Subj.* **2010**, *1800*, 745; c) N. Gálvez, B. Fernández, P. Sánchez, R. Cuesta, M. Ceolín, M. Clemente-León, S. Trasobares, M. López-Haro, J. J. Calvino, O. Stéphan, J. M. Domínguez-Vera, *J. Am. Chem. Soc.* **2008**, *130*, 8062; d) C. Quintana, J. M. Cowley, C. Marhic, *J. Struct. Biol.* **2004**, *147*, 166.
- [8] J. Joshi, A. Zimmerman, *Toxicology* **1988**, *48*, 21.
- [9] a) P. M. Harrison, P. Arosio, *Biochim. Biophys. Acta* **1996**, *1275*, 161; b) N. Bresgen, P. Eckl, *Biomolecules* **2015**, *5*, 808.
- [10] N. D. Chasteen, P. M. Harrison, *J. Struct. Biol.* **1999**, *126*, 182.
- [11] a) V.-A. Maraloiu, F. Appaix, A. Broisat, D. Le Guellec, V. S. Teodorescu, C. Ghezzi, B. van der Sanden, M.-G. Blanchin, *Nanomedicine* **2016**, *12*, 191; b) J. D. Lopez-Castro, A. V. Maraloiu, J. J. Delgado, J. J. Calvino, M. G. Blanchin, N. Galvez, J. M. Domínguez-Vera, *Nanoscale* **2011**, *3*, 4597.
- [12] a) I. Lynch, K. A. Dawson, *Nano Today* **2008**, *3*, 40; b) C. D. Walkey, W. C. W. Chan, *Chem. Soc. Rev.* **2012**, *41*, 2780.
- [13] F. Bertoli, G.-L. Davies, M. P. Monopoli, M. Moloney, Y. K. Gun'ko, A. Salvati, K. A. Dawson, *Small* **2014**, *10*, 3307.
- [14] S. J. Soenen, W. J. Parak, J. Rejman, B. Manshian, *Chem. Rev.* **2015**, *115*, 2109.
- [15] a) N. Liu, Y. Mu, Y. Chen, H. Sun, S. Han, M. Wang, H. Wang, Y. Li, Q. Xu, P. Huang, Z. Sun, *Part. Fibre Toxicol.* **2013**, *10*, 37; b) A. M. Derfus, W. C. W. Chan, S. N. Bhatia, *Nano Lett.* **2004**, *4*, 11.
- [16] R. P. Singh, P. Ramarao, *Toxicol. Lett.* **2012**, *213*, 249.
- [17] W.-S. Cho, R. Duffin, S. E. M. Howie, C. J. Scotton, W. A. H. Wallace, W. MacNee, M. Bradley, I. L. Megson, K. Donaldson, *Part. Fibre Toxicol.* **2011**, *8*, 27.
- [18] a) M. Levy, F. Lagarde, V. A. Maraloiu, M. G. Blanchin, F. Gendron, C. Wilhelm, F. Gazeau, *Nanotechnology* **2010**, *21*, 395103; b) A. S. Arbab, L. B. Wilson, P. Ashari, E. K. Jordan, B. K. Lewis, J. A. Frank, *NMR Biomed.* **2005**, *18*, 383; c) S. J. H. Soenen, U. Himmelreich, N. Nuytten, T. R. Pisanic, A. Ferrari, M. De Cuyper, *Small* **2010**, *6*, 2136.
- [19] M. Ghosh, F. Carlsson, A. Laskar, X.-M. Yuan, W. Li, *FEBS Lett.* **2011**, *585*, 623.
- [20] a) T. Kurz, B. Gustafsson, U. T. Brunk, *Free Radical Biol. Med.* **2011**, *50*, 1647; b) T. Kurz, A. Terman, B. Gustafsson, U. T. Brunk, *Histochem. Cell Biol.* **2008**, *129*, 389.
- [21] M. A. Krenn, M. Schürz, B. Teuffl, K. Uchida, P. M. Eckl, N. Bresgen, *Free Radical Biol. Med.* **2015**, *80*, 48.
- [22] J. D. Mancias, X. Wang, S. P. Gygi, J. W. Harper, A. C. Kimmelman, *Nature* **2014**, *509*, 105.
- [23] Y. Javed, L. Lartigue, P. Hugounenq, Q. L. Vuong, Y. Gossuin, R. Bazzi, C. Wilhelm, C. Ricolleau, F. Gazeau, D. Alloyeau, *Small* **2014**, *10*, 3325.
- [24] F. Gazeau, V. Shilov, J.-C. Bacri, E. Dubois, F. Gendron, R. Perzynski, Y. L. Raikher, V. I. Stepanov, *J. Magn. Magn. Mater.* **1999**, *202*, 535.
- [25] Y. Gossuin, P. Gillis, A. Hocq, Q. L. Vuong, A. Roch, *Wiley Interdiscip. Rev.: Nanomed. Nanobiotechnol.* **2009**, *1*, 299.
- [26] Z. Yang, X. Wang, H. Diao, J. Zhang, H. Li, H. Sun, Z. Guo, *Chem. Commun.* **2007**, *33*, 3453.
- [27] J.-W. Kim, S. H. Choi, P. T. Lillehei, S.-H. Chu, G. C. King, G. D. Watt, *Chem. Commun.* **2005**, *32*, 4101.
- [28] a) F. C. Meldrum, V. J. Wade, D. L. Nimmo, B. R. Heywood, S. Mann, *Nature* **1991**, *349*, 684; b) E. Fantechi, C. Innocenti, M. Zanardelli, M. Fittipaldi, E. Falvo, M. Carbo, V. Shullani, L. Di Cesare Mannelli, C. Ghelardini, A. M. Ferretti, A. Ponti, C. Sangregorio, P. Ceci, *ACS Nano* **2014**, *8*, 4705; c) J. C. Cutrin, S. G. Crich, D. Burghelena, W. Dastrù, S. Aime, *Mol. Pharmaceutics* **2013**, *10*, 2079.
- [29] S. Pead, E. Durrant, B. Webb, C. Larsen, D. Heaton, J. Johnson, G. Watt, *J. Inorg. Biochem.* **1995**, *59*, 15.
- [30] Y.-H. Pan, G. Vaughan, R. Brydson, A. Bleloch, M. Gass, K. Sader, A. Brown, *Ultramicroscopy* **2010**, *110*, 1020.
- [31] A. Luciani, S. Dechoux, V. Deveaux, M. Poirier-Quinot, N. Luciani, M. Levy, S. Ballet, S. Manin, C. Pechoux, G. Autret, O. Clément,

- A. Rahmouni, A. Mallat, C. Wilhelm, S. Lotersztajn, F. Gazeau, *Radiology* **2012**, 263, 786.
- [32] R. Massart, *IEEE Trans. Magn.* **1981**, 17, 1247.
- [33] L. Lartigue, C. Wilhelm, J. Servais, C. Factor, A. Dencausse, J.-C. Bacri, N. Luciani, F. Gazeau, *ACS Nano* **2012**, 6, 2665.
- [34] C. Ricolleau, J. Nelayah, T. Oikawa, Y. Kohno, N. Braidy, G. Wang, F. Hue, L. Florea, V. Pierron Bohnes, D. Alloyeau, *Microscopy* **2013**, 62, 283.

Received: June 17, 2016  
Revised: September 23, 2016  
Published online: